X-ray Structural Studies of Poly(3-alkylthiophenes): An Example of an Inverse Comb

T. J. Prosa and M. J. Winokur*

Department of Physics, University of Wisconsin, Madison, Wisconsin 53706

Jeff Moulton,† Paul Smith,† and A. J. Heeger‡

Departments of Materials Science and Physics, University of California, Santa Barbara, California 93105

Received February 4, 1992; Revised Manuscript Received April 30, 1992

ABSTRACT: X-ray diffraction studies of oriented poly(3-*n*-alkylthiophene) (P3AT's) solution-cast films show that these samples are characterized by well-organized lamellar structures whereby stacks of planar thiophene main chains are uniformly spaced by the alkyl side chains. In spite of considerable hydrocarbon chemical bonding and conformational disorder, a high degree of structural regularity is observed with appreciable three-dimensional ordering of the polymer chains. Analysis of the resultant scattering data in combination with model structure factor calculations leads to suggestive models in which an open packing of the alkyl chains is maintained with considerable side-chain disorder and side-chain mobility. There is evidence that this flexibility allows for an additional ordering process to occur at the interface formed by the alkyl side-chain end groups and that the liquid crystalline behavior is intimately related to the appearance of this structure.

I. Introduction

The study of electroactive polymers continues to be an area of intense interest for fundamental reasons as well as for technological applications.[1] Continued advances in both the synthesis and processing of these materials have dramatically improved the intrinsic sample characteristics and also the availability of new compounds.[2] One singularly important chemical modification has been the addition of saturated hydrocarbon alkyl or alkoxy side chains to the polymeric backbone.[3] This alteration imparts modest solubility to previously intractable host materials (e.g., polythiophene and polypyrrole) while still allowing for retention of their basic electronic properties. Thus this class of conducting polymers can be investigated while in solution,[4,5] when incorporated into macromolecular assemblies,[6] or when cast and drawn using traditional polymeric processing techniques.[7]

A large proportion of conducting polymer research has been directed toward understanding the electronic properties. Parallel investigations of structure have tended to lag because of inherent structural limitations in these materials. Many conducting polymers are characterized by multiple phases, by minimal crystalline fractions, and by small coherence lengths within crystalline portions of the sample. Intrinsic disorder effects such as paracrystallinity[8] can further complicate structural analyses. However, the molecular organization at the microscopic level necessarily impacts any comprehensive evaluation of their electronic properties. One well-known effect, common to highly conjugated polymeric materials, is a shift in the visible–ultraviolet absorption spectra due to deviations from backbone planarity concurrent with a reduction in the overall effective conjugation length. Alkyl-substituted polythiophenes,[4] polysilanes,[9,10] and various polydiacetylenes[11,12] all manifest pronounced solvatochromic and thermochromic responses.

Additionally this alkyl chain substitution, as well as synthesis methodology and processing, profoundly influences the resulting polymer microstructure. Chemically synthesized polythiophene powder samples are moderately crystalline, having a compact planar thiophene structure with four monomers per unit cell.[13] Electrochemically synthesized polythiophene or poly(3-methylthiophene) samples can exhibit helical configurations of the polymer strands which then may either close pack into a triangular array of these helices[14] or form superhelices.[15] Longer alkyl chain substitution restores a planar alternating zigzag conformation to the backbone.[16-20] These latter materials then form layered, semicrystalline structures whereby the alkyl side chains function as spacers between stacks of the polymer main chains (see Figure 1). The origin of this response arises from both steric packing constraints and from chemical compatabilities. Many of these proposed models have the average direction of the alkyl side-chain orientation parallel to the layer spacing and thereby require extensive interlayer alkyl-chain interdigitation. An alternative model incorporates a reorientation of the alkyl chain away from this direction.[21,22] While the nominal lamellar construction is now well established, detailed knowledge of the actual side-chain organization into an ordered matrix remains incomplete.

This lamellar structural organization is also common to conventional stiff-backboned polymers having undergone side-chain substitution by alkyl groups and is somewhat reminiscent of the comblike liquid crystalline polymers in which soft flexible main chains have had hard-segment side-group mesogens chemically coupled to the backbone.[23] In this context poly(3-alkylthiophenes) may be considered representative of an "alternating inverse comb". Recent observations show that P3AT's also undergo thermotropic transitions to a liquid crystalline state.[20,24] Thus structural studies of these electroactive materials can complement other, more general investigations[10,25,26] of alkyl-chain substitution on overall polymer structure. From this perspective, conducting polymers are especially interesting because their ability for dopant uptake may be viewed as an unusual mechanism by which the polymer structural organization is readily perturbed.[21]

In this paper we present data and structural analysis from an X-ray diffraction study of stretch-oriented solution-cast films of poly(3-*n*-hexylthiophene) (P3HT), poly(3-*n*-octylthiophene) (P3OT), and poly(3-*n*-dodecylthiophene) (P3DDT). Our studies show that processing of

† Department of Materials Science, University of California.
‡ Department of Physics, University of California.

0024-9297/92/2225-4364$03.00/0

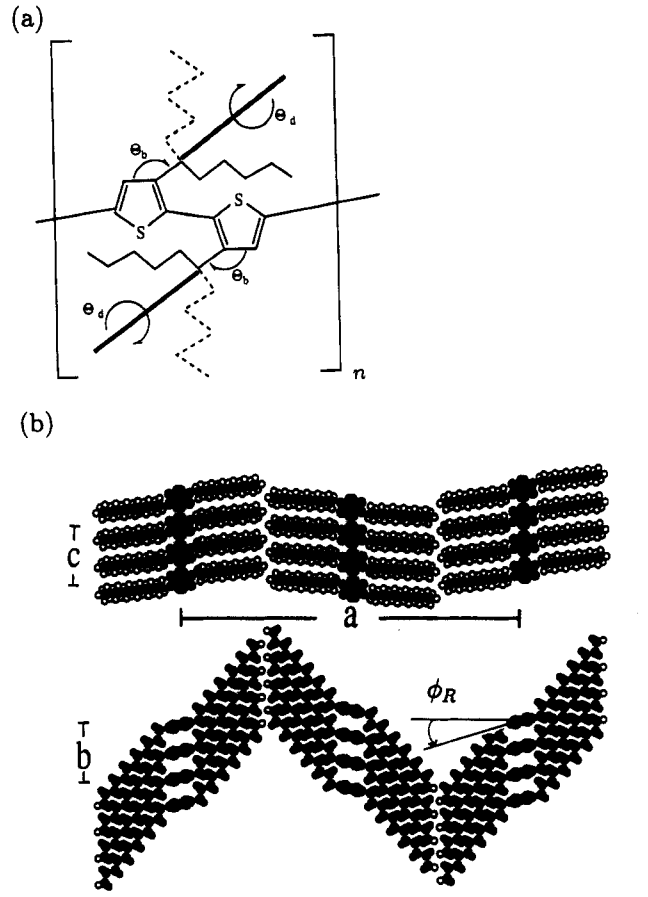

Figure 1. (a) Chemical structure of P3AT's. (b) Two different projections which show the lamellar packing of the P3AT's.

P3HT, P3OT, and P3DDT films can lead to a full three-dimensional (3D) texturing of the polymer structure. A description of this anisotropy is presented in combination with an overview of the X-ray scattering features characteristic to stretch-oriented P3AT samples. In general, all P3AT samples in this study exhibited the stacked lamellar morphology of Figure 1. This organization can allow for appreciable π-orbital overlap between adjacent chains although another structural organization, with much reduced overlap, has been reported for poly(3-decylthiophene).[13] We find that longer alkyl-chain substitution tends to enhance the overall interlayer structural ordering with improvements in the equatorial coherence lengths. In contrast, there is a systematic reduction in the perfection of the side-chain ordering. By analyzing our X-ray scattering data in tandem with structure factor calculations of suggestive models, we extend the scope of previous structural studies and address the full three-dimensional molecular organization within these compounds. These calculations support a model in which there is a tilted packing of the side chains with a singular absence of appreciable interlayer alkyl-chain interdigitation. This organization occurs in spite of, or perhaps as a result of, the presence of local side-chain disorder which is manifestly present in our samples. To attain a more realistic representation of the actual structure, we have performed structure factor calculations of models which incorporate some aspects of the chemical bonding disorder. Further P3DDT analysis, at reduced and at elevated temperatures, also allows for an interpretation of the thermally induced structural reorganizations.

II. Experimental Technique

The X-ray scattering data presented in this paper utilized polymer samples synthesized by Neste Oy (P3OT) and at Santa Barbara (P3HT and P3DDT) by direct oxidative coupling of the respective 3-alkylthiophene with $FeCl_3$.[27] The molecular weights were typically M_w = 80 000 and M_n = 20 000. After synthesis, the $FeCl_3$ was extracted and the films were dissolved in chloroform. These solutions were then filtered and immediately poured directly onto glass slides. After solvent evaporation, the films were lifted by methanol and clamped into a simple stretching device. Uniaxial stretching ratios as high as 4:1 were achieved at drawing temperatures ca. 100 °C.[28] Other casting conditions were examined, as noted in the text, without dramatic changes in the diffraction profiles.

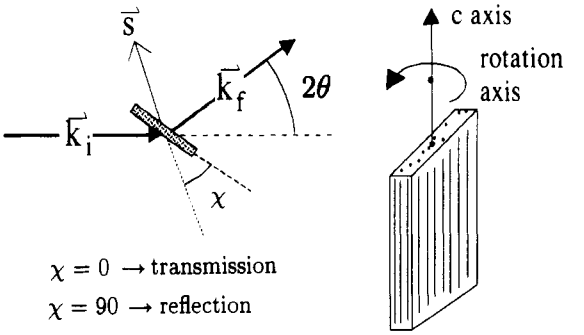

Figure 2. Schematic showing the geometry used for obtaining the equatorial anisotropy of P3AT cast films.

These cast and stretched films were then cut, stacked, and mounted into a holding cell. For elevated temperature studies the samples were placed into a home-built furnace equipped with resistive cartridge heaters and a three-term PID temperature controller (Omega CN2010). For reduced temperature studies, the samples were mounted to the cold-finger of a closed-cycle He cryostat equipped with a beryllium windowed vacuum shroud.

The X-ray diffraction facility consisted of an X-ray source, computer-controlled diffractometer (Huber D424/D511), and a linear array detector. The X-ray generator, a 15-kW Elliot GX-21 rotating anode, utilized a copper target ($\lambda_{K\alpha}$ = 1.542 Å) fitted with a bent graphite monochromator. The cross-sectional area of the incident X-ray beam at the sample was adjusted to ≈2.0 × 2.0 mm². The position-sensitive array detector consisted of a refrigerated silicon diode array (EG&G XR1412) and associated interface electronics (EG&G M1461). The detector's spatial resolution was set by forming 16 pixel groups from the detector's 960 accessible 25 μm × 2 mm pixels. This diode array was located ~30 cm from the scattering center and subtended a 2θ arc of ~4.5°. Typical counting rates, for a single group at the most intense reflection of 40-μm-thick undoped samples, were in excess of 25 counts per second (cps) per 16 pixel group. In the best case, a 200-μm multilayer stack gave integrated count rates exceeding 2000 cps for the most intense scattering features. In order to minimize nonlinearities across the detector, a correction factor for each group was included and the 2θ step size for each individual data collection point was limited to 0.5°.

In all cases, radial θ–2θ scans were performed with the sample mounted within the Eulerian cradle. By repositioning the sample, both the equatorial and nonequatorial scattering could be acquired. To examine the anisotropy within the equatorial plane (see Figure 2), sequential radial scans were executed with the samples rotated at 10° or 15° increments about the *c*-axis. For nonequatorial scattering, the sample was maintained in a symmetrical transmission geometry and the *c*-axis angle, with respect to the scattering plane of the detector, set at 6° (or 10°) increments from parallel to perpendicular. The resulting data were then mapped into a single image by drawing constant-intensity contours. These data approximate one quadrant of a typical flat-film photograph but without the geometrical distortions intrinsic to this film technique.

III. Experimental Results and Discussion

A. Scattering Features and Anisotropy of Processed Films. Example stretch-oriented P3HT, P3OT, and P3DDT constant X-ray intensity contour maps are displayed in parts a–c of Figure 3, respectively. In all

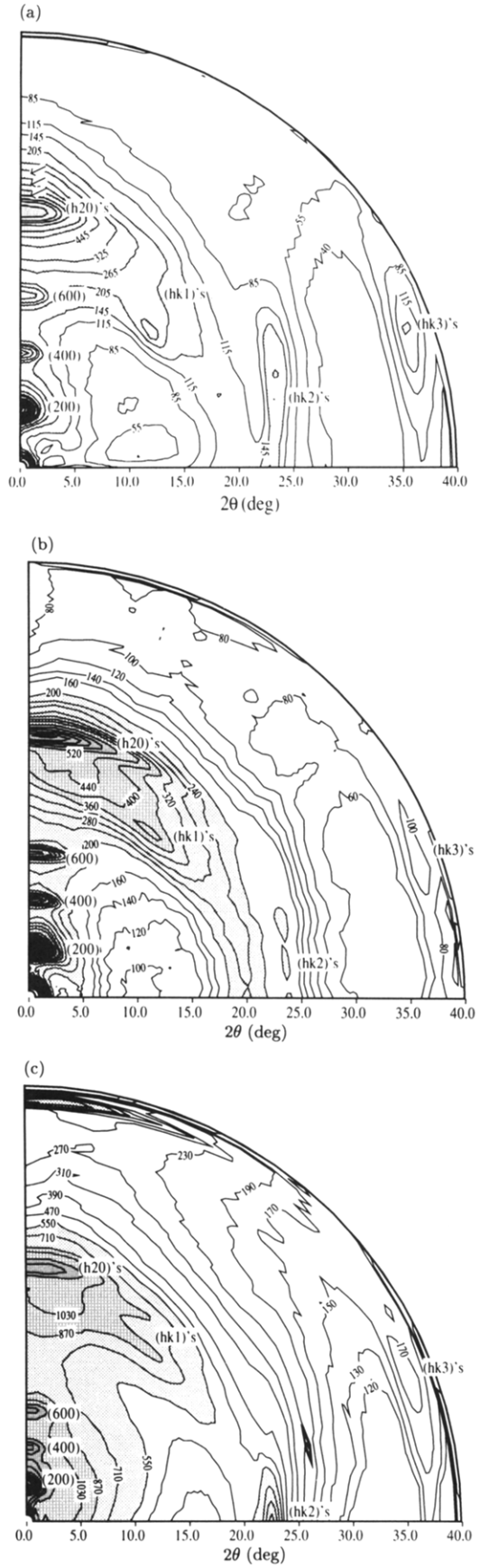

Figure 3. Contour maps of constant X-ray intensity between the equatorial ($hk0$) plane and the c-axis for stretch-oriented (a) P3HT, (b) P3OT, and (c) P3DDT samples. In all cases the ($hk0$) plane is vertical and the c-axis is horizontal.

cases the c-axis of the polymer is horizontal and the equatorial plane lies along the vertical. In general, only a total of 6–10 localized scattering features are individually resolved. The most obvious equatorial features are the three (or four) scattering peaks located at low angles [labeled (200), (400), (600), and so on in Figure 3a–c] along the equatorial direction. These reflections arise from the first-, second-, and higher-order reflections from the large-length 16.8, 20.6, and 25.9-Å interlayer d-spacing of P3HT, P3OT, and P3DDT, respectively. Sample-to-sample variations in this value were found to be ≈2%. From measurements of the azimuthal angular full width at half-maximum, the c-axis mosaic spread is ~15°. Since the degree of polymerization is relatively low, significant improvements in this orientation may be possible by drawing films of higher molecular weight. The other major equatorial feature [labeled as (h20)'s] is a broad "peak" centered at 23.4° and roughly corresponds to an intralayer chain-to-chain stacking distance of 3.8 Å.

Scattering intensities from evenly spaced l = 1, 2, and 3 layers are also apparent in these contour maps, and this distance corresponds to a ≈7.9-Å repeat along the chain axis (or c-axis) of the polymer. Along the l = 1 layer, two or three identifiable scattering features can be resolved [labeled as (hk1)'s]. These features, in combination with the absence of scattering along the meridional direction, indicate that 3D interchain correlations are present. For the l = 2 layer line, most of the scattering intensity is localized along or near the c-axis direction. In the case of P3HT and P3OT, flat-film photographs with slightly higher resolution are able to distinguish a series of closely spaced reflections in this l = 2 layer line,[29] further evidence for bulk ordering of these polymer compounds. For P3HT, a considerable portion of the l = 2 scattering intensity lies off the c-axis direction so that analysis of meridional scans may lead to anomalously short c-axis repeats.[19]

All of these localized scattering features rest atop diffuse scattering halos centered at low 2θ angle and about 2θ = 22°. Scans to higher angles resolve additional amorphous scattering features.[30] Previous studies indicate that at least two different structural components are present in P3AT samples. The small-angle halo (which is quite weak) arises primarily from packing of the polymer chains in disordered and/or "amorphous" regions[16] while the wide-angle halo is thought to arise from hydrocarbon structural disorder within all portions of the films. At least three sources of alkyl-chain disorder can be identified: head-to-head side-chain bonding, disruption of the alternating thiophene units, and side-chain conformational disorder (both static and thermal). These are depicted in Figure 4. NMR studies suggest that up to 25% of the alkyl chains are configured with head-to-head bonding arrangements.[18] There is also a systematic increase in the relative proportion of the wide-angle halo intensity with elongation of the P3AT alkyl-chain length. Qualitatively, this implies that there is an increase in the overall hydrocarbon disorder within the longer alkyl-substituted materials.

In addition to the uniaxial anisotropy induced by tensile drawing, the cast films themselves may also exhibit anisotropy. Two constant X-ray intensity contour maps, within the equatorial plane of representative stretched P3HT and P3DDT samples, are shown in Figure 5. In these films the large-length interlayer repeat is oriented approximately 45–60° away from the surface parallel with an equatorial mosaic of ~40°. The scattering feature centered at 2θ = 23.4° has a broader angular profile and is most intense for the scattering vector perpendicular to the surface normal. If these d-spacings are representative of the interlayer and intralayer spacings, respectively, then the broad 23.4° feature represents a collection of closely spaced peaks from a projected two-dimensional unit cell

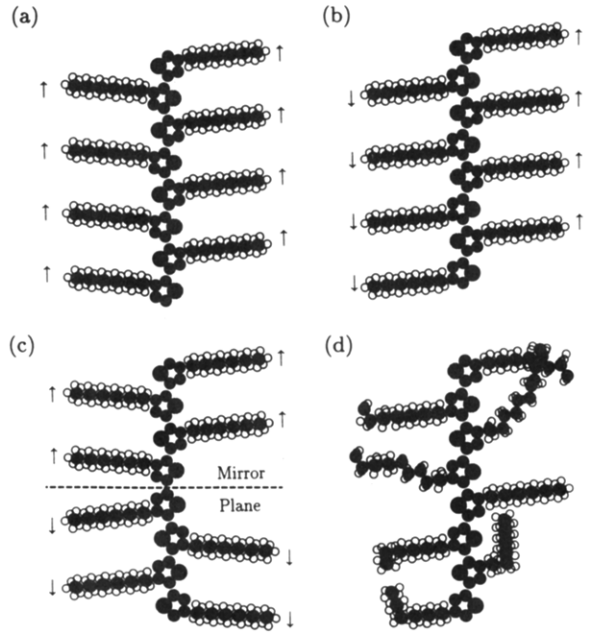

Figure 4. Various possible organizations of the monomer units in P3AT's: (a) ideal head-to-tail bonding configuration, (b) alternating head-to-head and tail-to-tail bonding configuration, (c) example of a reflection asymmetry in which the thiophene ring trans alternation is disrupted, (d) example of alkyl-chain disorder.

with nearly orthogonal axes. Inspection of the high-angle side of this peak in Figure 3a (denoted by arrows) also identifies weak striations in the scattering profiles of P3DDT. We have investigated and tentatively identified the origin of this equatorial anisotropy by varying both the solvent and substrate during moderately rapid casting. The only consistent finding is that macroscopic stresses arising from anisotropic shrinkage during the casting process are responsible. When casting on glass substrates, the films shrink dramatically in thickness but are constrained in their overall area. Hence, mechanical processing seems the most likely method which will yield improved 3D texturing of cast films. This is in contrast to the centrifuged precipitates of marginal solutions which exhibit pronounced intrinsic anisotropic morphological properties.[31]

In Figure 6 (or Figure 7), the individual layer line intensity profiles have been extracted from the P3DDT contour map and plotted as a function of the Bragg scattering angle, 2θ. The $l = 0$ profile is representative of the projected polymeric structure orthogonal to the polymer chain axis. The dramatic intensity reduction between the (200) and (400) reflections results primarily from the $1/\sin\theta^2$ functionality of the Lorentz factor (as discussed in the next section). Additionally, we note the relatively narrow radial widths of these reflections. Using the Debye–Scherrer relation as applied to the (200) reflection, an estimated 180-Å coherence length for this P3DDT sample is obtained. For the P3OT sample (in Figure 8) the coherence length becomes 240 Å, and for the P3HT sample (in Figure 9) this value is 170 Å. There is also a functional increase in the relative widths of the various high-order (h00) reflections with increasing h. This suggests that strain and/or paracrystallinity effects are present.[8] A quantitative analysis was not undertaken since only three reflection orders could be clearly resolved.

B. Structural Characteristics and Modeling of P3AT's. 1. Calculation of WAXS Diffraction Profiles. Calculation of wide-angle X-ray scattering profile intensities for comparison with polymer film and

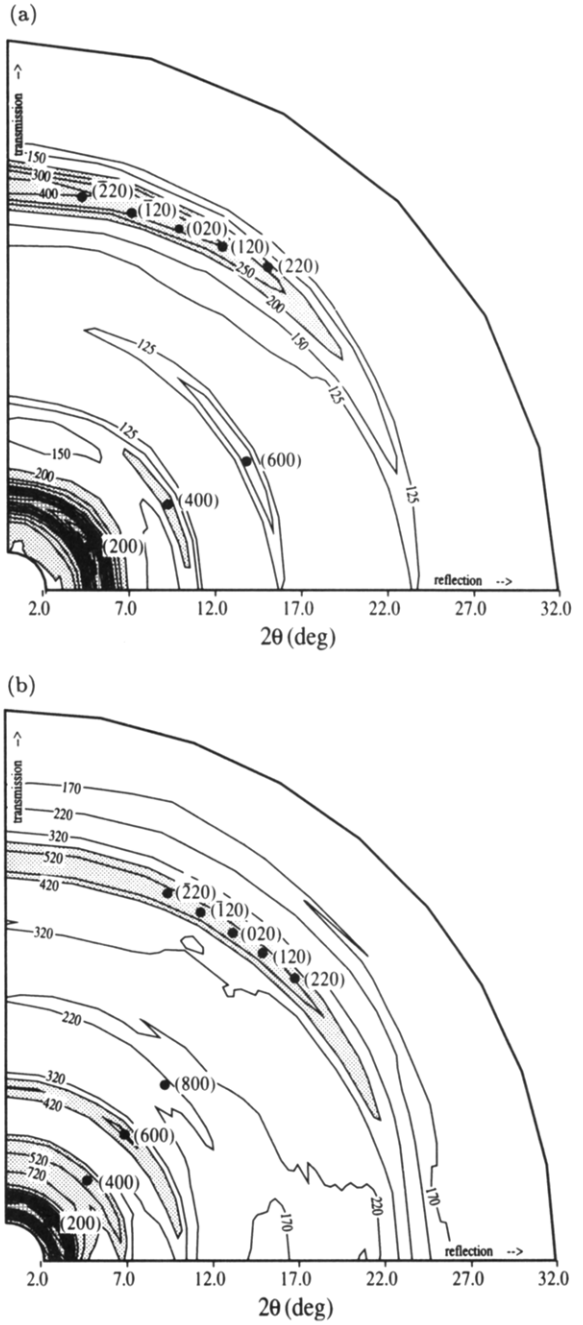

Figure 5. Contour maps of constant X-ray intensity about the equatorial plane from transmission to reflection geometry (as indicated by Figure 2) for selected (a) P3HT and (b) P3DDT samples.

fiber diffraction data has a well-established methodology.[32] Due to the structural complexity intrinsic to these side-chain-substituted P3AT compounds, this study has been restricted to analysis of scattering features which arise from clearly represented periodicities in the polymer host. All other scattering features are treated collectively as constituents in various background profiles. Additionally, these models and subsequent structure factor calculations do not, as yet, incorporate intramolecular and intermolecular packing energies.

The method of computing X-ray structure factors closely follows the procedure outlined in ref 33. For all P3AT's studied we assume that there is an appropriate 3D unit cell in which the chain axis of the polymer lies parallel to the c-axis. All intramolecular atomic positions are considered invariant except for the introduction of a minimal set of free parameters. These are discussed in greater

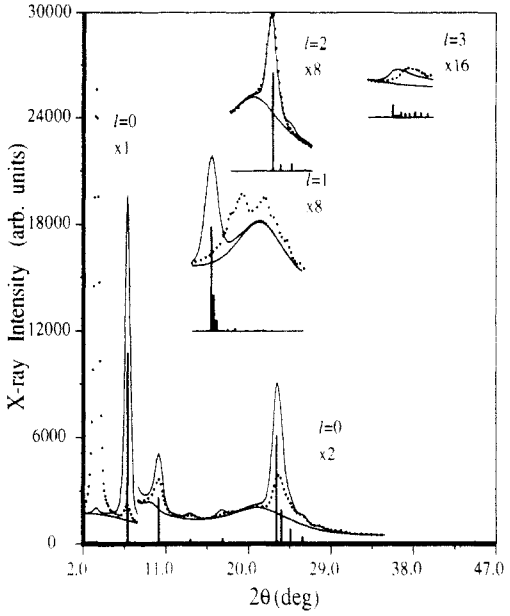

Figure 6. Experimental (dots) and calculated (lines) diffraction profiles (including background) for P3DDT using the lattice reflections (vertical bars) employing a model which assumes no main chain, $\phi_R = 0$, or side chain, $\theta_d = 0$, rotation. All $l \neq 0$ curves have been shifted for clarity.

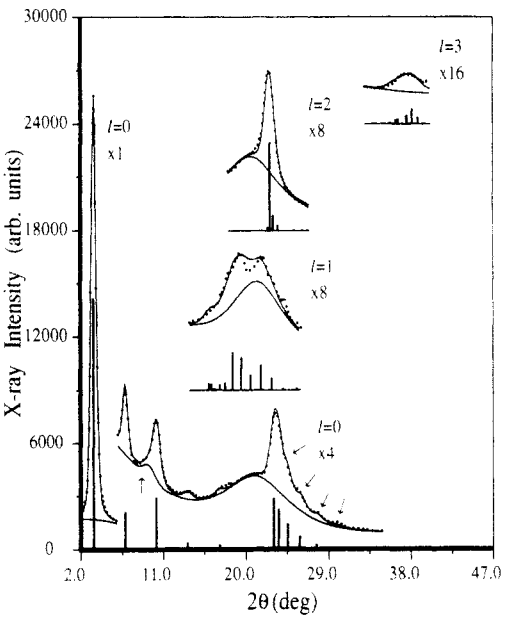

Figure 7. Experimental (dots) and calculated (lines) diffraction profiles for P3DDT according to the parameters displayed in Table I using the lattice reflections (vertical bars) superimposed on a background profile. The arrows about $2\theta \approx 25°$ identify various distinguishable (h20) reflections. The other arrow points to a weak scattering peak of unknown origin. All $l \neq 0$ curves have been shifted for clarity.

detail in the next section. Individual lattice reflection intensities, $I_{calc}(hkl)$, were calculated using

$$I_{calc}(hkl) = P(\theta)\, L(\theta)\, |F(hkl)|^2 \qquad (1)$$

where $F(hkl)$ is the structure factor, θ represents the Bragg angle, $P(\theta)$ is the polarization factor, and

$$L(\theta) = 1/\sin^2\theta \cos\theta \qquad (2)$$

is the Lorentz factor appropriate for powder samples. More complex forms of the Lorentz factor can be utilized for highly oriented polymer samples,[33] but the large c-axis mosaics in these P3AT samples limited their usefulness.

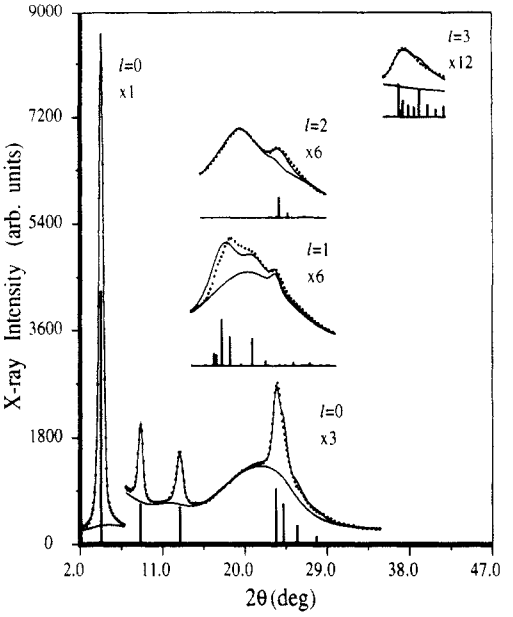

Figure 8. Experimental (dots) and calculated (lines) diffraction profiles for P3OT according to the parameters displayed in Table I using the lattice reflections (vertical bars) superimposed on a background profile. All $l \neq 0$ curves have been shifted for clarity.

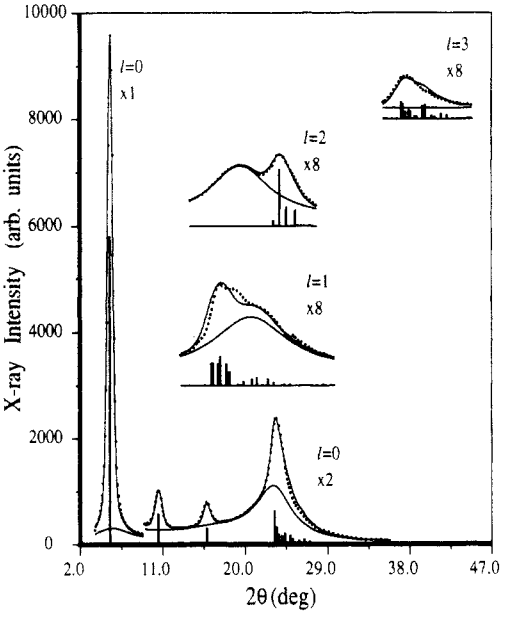

Figure 9. Experimental (dots) and calculated (lines) diffraction profiles for P3HT according to the parameters displayed in Table I using the lattice reflections (vertical bars) superimposed on a background profile. All $l \neq 0$ curves have been shifted for clarity.

Correction factors for changes in scattering volume were not employed. In the case $l = 0$ the samples were fully illuminated by the incident beam while for nonzero l this factor is, given our specific treatment and limitations of the experimental data, not generally necessary. The explicit form of the structure factor is

$$F(hkl) = \sum_{j=1}^{N} f_j(\sin\theta/\lambda) \exp(i\vec{G}_{hkl}\cdot\vec{r}_j) M(\vec{G}_{hkl}) \qquad (3)$$

in which there are N atoms within the unit cell, $\lambda = 1.542$ Å, $\vec{G}_{hkl}$ is a reciprocal lattice vector, $\vec{r}_j$ is the position of the jth atom, f_j is the atomic form factor,[34] and $M(\vec{G}_{hkl})$ is an anisotropic Debye temperature factor. The actual values for Debye parameters are, at best, qualitative and are not explicitly stated in the text. In addition, the actual number of requisite Fourier sums can be reduced by taking

advantage of any translational symmetries between chemical subunits within the lattice basis.

As a result of the large unit cells employed, all structure factor calculations exhibited many closely spaced lattice reflections which were necessarily superimposed. Rather than perform a deconvolution of this data[35] or direct comparison with the entire experimentally obtained constant intensity contour maps,[36] a customized hybrid procedure was implemented that achieved reasonable computational turnaround times so that a variety of structural models and subtle modifications could be rapidly investigated. In general, all nonzero intensity lattice reflections, $I_{calc}(hkl)$ were convoluted with a combined Lorentzian and Gaussian function

$$C(2\theta)_{hkl} = s \exp\left[-4 \ln 2\left(\frac{2\theta - 2\theta_{hkl}}{w}\right)^2\right] + (1-s)\frac{1}{1+4\left(\frac{2\theta - 2\theta_{hkl}}{w}\right)^2} \quad (4)$$

where s is the relative Gaussian–Lorentzian weighting, w is the full width at half-maximum of the peak, and θ_{hkl} is the Bragg angle of a particular reflection. The calculated radial profiles for each given l layer line were obtained using

$$I_{calc}(2\theta) = \sum_{hkl} \sum_{2\theta_{min}}^{2\theta_{max}} I(hkl)\, C(2\theta)_{hkl}/d_{hkl} + B_l(2\theta) \quad (5)$$

where $B_l(2\theta)$ is an arbitrary and slowly varying background profile. The widths, d_{hkl}, of the isolated scattering features were adjusted independently (or by using a functionalized peak to peak coupling) while an average fixed width was assumed for all superimposed lattice reflections. This composite calculated scattering profile, combined with an appropriate background, could then be compared directly with scattering data from various layer lines which had been extracted from the constant X-ray intensity contour maps. Initially only the equatorial ($hk0$) scattering data were examined, but then weighted (and appropriately scaled) $l = 1$, 2, and 3 layer line profiles were incorporated into the fitting procedure. The relative deviation, R, was minimized according to the expression

$$R = \frac{\sum_l \sum_{2\theta} (I_{calc} - I_{exptl})^2 W(l,2\theta)}{\sum_l \sum_{2\theta} (I_{exptl})^2 W(l,2\theta)} \quad (6)$$

where W is a relative weighting factor. It is important to note that the $l \neq 0$ scattering profiles are presented with respect to the actual Bragg angle 2θ and not in terms of their component equatorial wavevector parallel to the ($hk0$) plane.

2. Modeling Results. The integrated intensity ratios of the various peaks are ultimately representative of the actual atomic positions. The general features of the scattering data support a planar conformation of the thiophene rings, and infrared absorption studies[16] suggest a large proportion of trans-planar bonding configurations for the alkyl side chains at room temperature. If these basic characteristics are rigidly enforced, then the only remaining allowed structural degrees of freedom are in the lattice parameters, rotation about the polymer chain axis (i.e., a setting angle, ϕ_R), rotation of the alkyl side chain about the C–C bond which connects to the thiophene backbone (a dihedral angle, θ_D), and, finally, changes in this C–C bond angle with respect to the chain axis direction, θ_B. These parameters are shown schematically in Figure 1. In reality the actual physical situation is expected to be considerably more complicated, and hence only the average direction of the alkyl side-chain orientation is of meaningful significance.

Since P3DDT samples exhibit scattering profiles which have the most well-defined ($hk0$) features [$h, k \neq 0$], they allow for a critical evaluation of the various degrees of freedom within the context of a comprehensive 3D unit cell. Nominally, a chain or c-axis repeat of 8.0 Å can be determined from the position of the various layer lines, and an approximate interlayer chain spacing of 3.8 Å can be estimated from the position of the 23.4° peak. The absence of measurable X-ray intensity along (or near) the meridional direction of both the $l = 1$ and $l = 3$ layer profiles implies that an oblique angling of neighboring alkylthiophene chains within individual stacks.[30] Because of the main-chain and side-chain interactions which impose this staggering within the individual layers, this ordering tends to dominate the formation of nonequatorial scattering features. Hence, ($0kl$) scattering peaks tend to be most clearly resolved. Recent work of Mardalen et al.[31] shows that qualitative agreement of the scattering intensities can be obtained if a model incorporating complete planar disorder between layers is employed. In this (our) paper, as well as that by Tashiro,[20] the alkylthiophene structure is approached from the alternative perspective of interlayer ordering. Clearly the actual situation must be intermediate to these two extremes.

Nonprimitive orthorhombic unit cells were typically employed, but lower symmetries were also investigated. The specific unit cell employs a doubling of the layer repeat so that both positive and negative chain axis rotations were equally represented in an esthetic manner. In general, the 2θ regions of interest for these calculated structure factors were not sensitive to this structural characteristic. This basic model also incorporates a doubling of the b-axis with a $c/2$ intralayer staggering of adjacent thiophene chains and suggests a higher symmetry configuration than that of ref 31. In full there are eight monomers per (nonprimitive and unconventional) unit cell.

If the plane formed by the side-chain backbone (assuming an all-trans conformation) is coplanar with that of the thiophene backbone, the observed 25.9-Å interlayer spacing in P3DDT requires either interdigitation from neighboring stacks or a tilting of the alkyl chains within a particular layer. In Figure 6 we display the calculated structure factor profiles for a model which includes no main-chain rotation and no side-chain reorientation away from the interlayer parallel. Clearly this model fails for all data except for scattering intensity along the $l = 2$ layer line. Simple rotations about the chain axis improve the intensity ratios of the ($h00$) reflections but do not achieve good agreement elsewhere.

Figure 7 displays the calculated structure factor using a structural model which best matches the $l = 0$, 1, 2, and 3 experimental scattering data. For this P3DDT sample the lattice parameters and other associated free parameters are listed in Table I. We again reiterate that the broadened 23.4° peak is a linear superposition of closely spaced ($h20$) reflections. Hence, the actual intralayer spacing is found to be 7.67 Å. Although there is considerable discretion in choosing an appropriate background, the specific functionality of the various layer lines is extremely well represented. Moreover, we note that there is considerable sensitivity to the actual choice of bond angle, setting angle, and dihedral angle. To match the measured absolute nonequatorial scattering intensities, a smaller scaling factor

Table I
Refined P3AT Unit Cell Parameters (T = 20 °C)

	lattice param				cell param (deg)			density (g/cm^3)	
sample	a (Å)	b (Å)	c (Å)	α (deg)	ϕ_R	θ_d	θ_b	calc	exptl
P3HT	33.6	7.66	7.7	90	5	89	105	1.12	1.10
P3OT	41.3	7.63	7.7	90	6	84	106	1.06	1.02
P3DDT[a]	51.9	7.74	8.0	90	13	82	100	1.03	1.01

[a] Values of a = 52.00 Å, b = 7.74 Å, c = 7.9 Å, and β = 86° provide a slightly improved fit.

(in this case, 0.5) has been used for all these lattice reflections. This implies that at least some scattering intensity has been transferred into the amorphous halo. Alternatively, we could employ an even more complex model which includes individual Debye factors for the various constituents or even a fractional occupancy by various atoms within the unit cell basis. At present either enhancement would yield only minimal improvements and would not substantially alter the overall quality of the actual fits or of our general conclusions.

It is interesting to note there is anisotropy in the 22° amorphous halo itself. Along the equatorial direction its intensity maximum is closest to 2θ = 22°, while along the c-axis it shifts to 21°. This implies that the alkyl-chain disorder is not isotropic but must be coupled to the orientation of the thiophene backbones and suggests that alkyl-chain disorder exists within both the ordered lamellar regions as well as within truly amorphous portions of the polymer.

Analogous calculations have been performed for both P3HT and P3OT samples. As a consequence of the shorter alkyl-chain lengths and correspondingly smaller unit cells, there should be more pronounced separations of the various reflections which comprise the nonequatorial scattering data. In general, these features tend to be more poorly resolved. For equatorial scans the ($hk0$) [h, $k \neq 0$] reflections were also less clearly distinguishable. This is due, in part, to the reduced coherence lengths of the shorter alkyl P3HT sample in combination with a theorized increase in the layer to layer fluctuations[30] (which typically yields the asymmetric Warren line shape). The best-fit unit cell parameters are compiled in Table I. In particular, P3HT is rather insensitive to the relative layer to layer positioning. Comparisons of the experimental profiles with those calculated are shown in Figures 8 and 9 for P3OT and P3HT respectively. As was the case for P3DDT, there is relatively good agreement between the experimental and calculated curves. In P3HT, layer lines up to l = 6 were also examined (not shown) with good results. Using these lattice parameters, the specific density of the polymer can be determined, and these values also compare favorably to those obtained experimentally by flotation techniques.

The amorphous halo, now centered nearer 23°, also shows the basic angular variations as seen in P3HT and P3OT samples with a gradual shift of approximately 3° as the scattering vector is changed from the equatorial to meridional directions. Surprisingly, the relative proportion of amorphous to "crystalline" scattering is least in well-annealed P3HT samples. Thus, while the 3D organization is poorest in this compound, the fraction of hydrocarbon disorder is lowest. This seeming contradiction can be qualitatively explained by suggesting that there must be two independent ordering processes which occur within these lamellar systems. The first involves stacking of the thiophene chains to yield a nested alkyl packing. The second is an additional ordering of the hydrocarbon chain ends. For the P3DDT, the additional conformational flexibility available allows for improved end-group packing with a net disruption of the alkyl-chain ordering. In support of this secondary "crystallization" is the presence of endothermic peaks (on heating) in differential scanning calorimetry scans of P3DDT[20] at temperatures near 50 °C.

The increased side-chain disorder within the longer alkyl P3AT samples implies that the head-to-tail coupling disorder along the thiophene main chains is a relatively unimportant factor in the overall 3D ordering process. In fact, the models of Figures 7–9 all employ alternating head-to-head, tail-to-tail alkyl linkages between the two thiophene units on a chain (see Figure 4b). Slightly poorer fits for the l = 1 layer lines are obtained with conventional head-to-tail linkages. Similarly, superstructures incorporating three head-to-tail linkages for every one head-to-head (or tail-to-tail), and thereby approximating the experimentally determined bonding disorder, also give equally acceptable fits. Consistent with the presence of this structural inhomogeneity is the persistence of a weak, broad scattering feature centered near 2θ = 4.5° in meridional scans, parallel to the polymer chain axis, for P3HT, P3OT, and P3DDT samples. This peak corresponds to a repeat of 15 Å or nearly every four monomer units.

The existence of an additional structural ordering at the side-chain ends may also suggest a possible explanation for the absence of 3D crystallization in structurally related compounds. For instance, di-n-alkyl,alkyl'polysilanes do not form 3D structures if the alkyl-chain mismatch is by more a one CH_2 unit.[37] As a further example we note that the mesomorphic properties of all-hydrocarbon polymers which contain biphenyl mesogens are also extremely sensitive to the side-chain tail lengths.[38] Materials in which the end-group ordering process is disrupted are unable to form three-dimensionally ordered materials.

While our primitive model cannot reproduce the characteristic scattering features arising from disorder in the P3AT samples, it does accurately model the intensity variations along the layer lines for any well-defined periodicities. The single most important feature of the 3D interlayer ordering is in the relative positioning of the alkyl chains. For P3DDT, the nesting of adjacent stacks tends to position the alkyl chains as shown in Figure 1b with a well-defined staggering of the chain ends in the a–c plane and a more subtle positioning within the a–b plane. In this construction the relative interlayer shift parallel to the b-axis is by $b/4$.

C. Temperature-Dependent Studies. Since P3DDT exhibits the most pronounced 3D organizational features, the equatorial ($hk0$) scattering profiles were also examined at both elevated and reduced temperatures. On heating, P3DDT has been found to undergo a transition to a liquid crystalline state in which only the equatorial reflections remain.[20] The experimental scattering profiles are shown in Figure 10 in comparison with the best-fit structure factor calculations at selected temperatures. In general, most of the observed changes are consistent with variations in the lattice constants. There is a slight systematic failing of the proposed model at reduced temperatures. In short, the best-fit lattice parameters do not give entirely satisfactory fits to the pronounced features of the region of 2θ

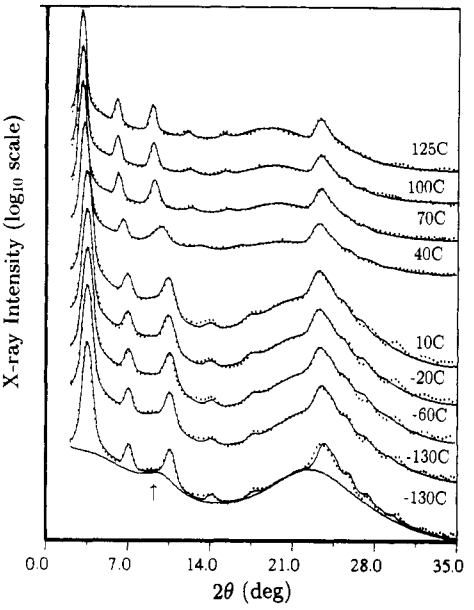

Figure 10. Experimental (dots) and calculated (lines) equatorial diffraction profiles for P3DDT at various indicated temperatures. Note that different samples were used for the elevated and reduced temperature runs. The arrow points to an additional temperature-sensitive scattering peak of unidentified origin. Also note that the bottom two profiles are the same experimental data but with different calculated profiles (see text).

Table II
Refined P3DDT Unit Cell Parameters

	lattice param		cell param (deg)		
temp (°C)	a (Å)	b (Å)	ϕ_R	θ_d	θ_b
		Sample 1			
−130	50.2	7.65	15	81	100
−80	50.1	7.68	15	81	100
−40	50.4	7.69	15	82	100
−20	50.7	7.69	14	82	101
0	50.8	7.73	14	82	102
20	51.1	7.72	14	82	102
		Sample 2			
25	52.5	7.75	13	82	100
40	53.9	7.73	11	83	100
55	55.6	7.67	9	78	102
70	57.4	7.67	7	77	102
85	57.8	7.67	6	77	102
100	58.0	7.67	6	76	102
115	58.3	7.67	5	76	102
125	58.6	7.67	5	76	102

between 25° and 28°. Decreasing the intralayer repeat b improves the fit to the experimental data in this portion of the spectrum (at the bottom of Figure 10) but then does not accurately reproduce the scattering intensity at a slightly lower 2θ angle. Table II contains a listing of the measured lattice parameters most consistent with the experimentally measured peak positions and various unit cell parameters as determined by structure factor calculations.

Thermal heating initiates a variety of significant structural changes. In addition to position shifts of the various equatorial reflections, there is a systematic increase in the intensity of the amorphous halo centered at 22°, indicative of the increased alkyl chain order, and a smooth shift to lower angle. The most dramatic changes occur in the vicinity of 50 °C. In particular, the intralayer spacing increases most rapidly in this temperature region while, somewhat surprisingly, the intralayer spacing exhibits a negative coefficient of thermal expansion. In addition, there is a notable loss of distinguishability in the ($hk0$) [h, $k \neq 0$] reflections. This alteration implies the loss phase coherence between adjacent alkylthiophene stacks. Increased temperature also causes a reduction in the intensity of a relatively weak scattering peak at 8.5° (as indicated by the arrows in Figures 7 and 10). The origin of this peak is still, at present, unknown.

These structure factor calculations imply that few internal unit cell changes (i.e., θ_b, ϕ_R, θ_d) occur at reduced temperature. Most variations in these parameters are confined to temperatures in the range of 25–70 °C. In this region there are reductions in both the polymer chain setting angle and in the dihedral angle. Nominally these shifts provide for the greater than average increases observed in the interlayer d-spacing.

Finally, P3DDT is also somewhat unusual in that there is an anomalous narrowing of the ($h00$) reflections on heating[20] which was not clearly observed in a similar study of P3HT samples.[16] In fact, the maximum coherence length is found to exceed 400 Å in this mesomorphic state or, equivalently, over 17 layer repeats. While some of this narrowing may be attributed to simple thermal annealing effects, there is still significant rebroadening of these profiles on cooling.

The existence of the aforementioned secondary ordering at the alkyl-chain ends provides a straightforward mechanism by which this last structural feature may be rationalized. In the context of competing interactions, enhanced local ordering at the layer interface enforces 3D ordering while disrupting the intralayer stacking of the alkyl chains and interfering with the long-range order along the layer perpendicular. Analogous transformations are found to occur in other low-dimensional composite materials in which competing interactions exist.[39] Melting of P3DDT is clearly a two-step process in which the increased side-chain motion, and a concomitant increase of gauche conformations, initially disrupts the local ordering at the alkyl-chain ends. The net result is a thermotropic mesophase characterized by decoupled free "floating" layers. This specific transition does not appear to strongly influence P3DDT's thermochromic properties since there are no anomalous changes in the UV–visible absorption spectra at these temperatures.[20] Continued alkyl-chain "melting" at higher temperatures eventually disrupts the lamellar stacking of the polymer itself, resulting in a true polymer melt. In contrast, the melting transformation of P3HT cast-film samples should not exhibit such clearly defined thermally derived steps because of the observed lack of clear 3D ordering. This difference may also give rise to distinct differences in the doping-induced structural transformations.[22] As a final comment we note that the sluggish structural kinetics on cooling seem to involve primarily ordering at the side-chain end groups.

IV. Conclusions

Through the use of structural models and detailed structure factor calculations we have obtained an enhanced understanding of the key aspects of structural ordering within one class of side-chain-substituted polymeric compounds. The principle result is that the side-chain orientation must include chain tilts away from the layer perpendicular which nearly eliminates interlayer alkyl-chain interdigitation. If this side-chain orientation is assumed, then all nonamorphous scattering features, equatorial and nonequatorial, can be accurately reproduced.

We have also presented evidence for the existence of a second structural feature intrinsic to P3AT's with longer alkyl side-chain lengths. Specifically, the data suggest

that an additional (and independent) structural ordering occurs at the alkyl-chain interface between adjacent alkylthiophene layers. The disruption of this interface destroys any appreciable interlayer ordering in P3DDT samples and gives rise to a liquid crystalline state with certain enhanced structural properties. P3HT does not show clear evidence of this ordering process while P3OT appears to be closest to the alkyl-chain length which defines a crossover region.

Acknowledgment. This work was supported by NSF DMR Grant No. DMR-8917530 (M.J.W.) and by ONR under N00014-91-J-1235 (J.M., P.S., and A.J.H.). Acknowledgment is also made to the donors of the Petroleum Research Fund, administered by the American Chemical Society, for partial support (T.J.P.) of this research.

References and Notes

(1) *Science and Applications of Conducting Polymers*; Salaneck, W. R., Clark, D. T., Samuelsen, E. J., Adam Hilger: Bristol, U.K., 1991.
(2) For the most recent International Conference on Synthetic Metals proceedings, see: *Synth. Met.* **1991**, *41–43*.
(3) Jen, K. Y.; Oboodi, R.; Elsenbaumer, R. L. *Polym. Mater. Sci. Eng.* **1985**, *53*, 79.
(4) Rughooputh, S. D. D. V.; Hotta, S.; Hegger, A. J.; Wudl, F. *J. Polym. Sci., Phys.* **1987**, *25*, 1071.
(5) Aimé, J. P.; Bargain, F.; Schott, M.; Eckhardt, H.; Miller, G. G.; Elsenbaumer, R. L. *Phys. Rev. Lett.* **1989**, *62*, 55.
(6) Watanabe, I.; Hong, H.; Rubner, M. F. *Langmuir* **1990**, *6*, 1164.
(7) Yoshino, K.; Nakajima, S.; Sugimoto, R. *Jpn. J. Appl. Phys.* **1987**, *26*, L1038.
(8) Hosemann, R.; Bagchi, S. N. *Direct Analysis of Diffraction by Matter*; North-Holland: Amsterdam, The Netherlands, 1962.
(9) Harrah, L. A.; Zeigler, J. M. *J. Polym. Sci. Polym. Lett. Ed.* **1985**, *23*, 209.
(10) Schilling, F. C.; Lovinger, A. J.; Zeigler, J. M.; Davis, D. D.; Bovey, F. A. *Macromolecules* **1989**, *22*, 3055.
(11) Patel, G. N.; Chance, R. R.; Witt, J. D. *J. Chem. Phys.* **1986**, *70*, 4387.
(12) Wenz, G.; Muller, M. A.; Schmidt, M.; Wegner, G. *Macromolecules* **1984**, *17*, 837.
(13) Brückner, S.; Porzio, W. *Makromol. Chem.* **1989**, *89*, 961.
(14) Garnier, F.; Tourillon, G.; Barraud, J. Y.; Dexpert, H. *J. Mater. Sci.* **1985**, *25*, 2687.
(15) Yang, R.; Evans, D. F.; Christensen, L.; Hendrickson, W. A. *J. Phys. Chem.* **1990**, *94*, 6117.
(16) Winokur, M. J.; Spiegel, D.; Kim, Y. H.; Hotta, S.; Heeger, A. J. *Synth. Met.* **1989**, *28*, C419.
(17) Gustafsson, G.; Inganäs, O.; Osterholm, H.; Laakso, J., to be published.
(18) Leclerc, M.; Diaz, F. M.; Wegner, G. *Makromol. Chem.* **1989**, *190*, 3105.
(19) Mårdalen, J.; Samuelsen, E. J.; Gautun, O. R.; Carlsen, P. H. *Solid State Commun.* **1991**, *77*, 337.
(20) Tashiro, K.; Ono, K.; Minagawa, Y.; Kobayashi, K.; Kawai, T.; Yoshino, K. *J. Polym. Sci., Polym. Phys.* **1991**, *29*, 1223.
(21) Winokur, M. J.; Wamsley, P.; Moulton, J.; Smith, P.; Heeger, A. J. *Macromolecules* **1991**, *24*, 3812.
(22) Winokur, M. J.; Prosa, T. J.; Moulton, J.; Smith, P.; Heeger, A. J. *Polym. Prepr. (Am. Chem. Soc., Div. Polym. Chem.)* **1992**, *33* (1), 296.
(23) Brostow, W. *Polymer* **1990**, *31*, 979.
(24) Tashiro, K.; Ono, K.; Minagawa, Y.; Kobayashi, K.; Kawai, T.; Yoshino, K. *Synth. Met.* **1991**, *41*, 571.
(25) Ballauff, M.; Rosenau-Eichin, R.; Fischer, E. W. *Mol. Cryst. Liq. Cryst.* **1988**, *155*, 211.
(26) Ballauff, M.; Berger, K. *Mol. Cryst. Liq. Cryst.* **1988**, *157*, 109.
(27) Inganäs, O.; Salaneck, W. R.; Osterholm, H.; Laakso, J. *Synth. Met.* **1988**, *22*, 395.
(28) Moulton, J.; Smith, P. *Synth. Met.* **1991**, *40*, 13.
(29) Moulton, J. D. Ph.D. thesis, University of California at Santa Barbara, 1991.
(30) Mårdalen, J.; Samuelsen, E. J.; Gautun, O. R.; Carlsen, P. H. *Solid State Commun.* **1991**, *80*, 9.
(31) Mårdalen, J.; Samuelsen, E. J. *Synth. Met.*, in press.
(32) Alexander, L. E. *X-ray Diffraction Methods in Polymer Science*; Wiley-Interscience: New York, 1969.
(33) de Wolff, P. M. *J. Polym. Sci.* **1962**, *60*, S34.
(34) *International Tables for X-ray Crystallography*; Kynoch Press: Birmingham, 1974; Vol. IV.
(35) Millane, R. P.; Arnott, S. *J. Macromol. Sci.* **1985**, *B24*, 193.
(36) Rutledge, G. C.; Suter, U. W.; Papaspyrides, C. D. *Macromolecules* **1991**, *24*, 1934.
(37) Klemman, B.; Koutsky, J., unpublished.
(38) Mallon, J. J.; Kantor, S. W. *Macromolecules* **1990**, *23*, 1249.
(39) Winokur, M. J.; Clarke, R. *Phys. Rev. Lett.* **1985**, *54*, 811.

Registry No. P3HT, 104934-50-1; P3OT, 104934-51-2; P3ODT, 104934-53-4.